Uncorrected Proof

Iran J Pharm Res. 2026; 25(1): e175904 https://doi.org/10.5812/ijpr-175904

Published Online: 2026 November 15 **Research Article**

Design, Synthesis, Cytotoxic Evaluation, and Molecular Docking Studies of Quinazolinone-Based Thioacetamide Derivatives as Potential Anticancer Agents

Sara Mansouri [1], Razieh Salehi Ashani [1], Sayyed Ali Tabatabai [2], Farzad Kobarfard [1,3], Elham Rezaee [1], Sayyed Abbas Tabatabai [1,3,*]

[1] Department of Pharmaceutical Chemistry, School of Pharmacy, Shahid Beheshti University of Medical Sciences, Tehran, Iran
[2] Department of Cellular and Molecular Biology, Faculty of Life Sciences and Biotechnology, Shahid Beheshti University, Tehran, Iran
[3] Phytochemistry Research Center, Shahid Beheshti University of Medical Sciences, Tehran, Iran

[*] ***Corresponding Author:*** Department of Pharmaceutical Chemistry, School of Pharmacy, Shahid Beheshti University of Medical Sciences, Tehran, Iran. Email: sa_tabatabai@yahoo.com

Received: 13 October, 2026; **Revised:** 8 November, 2026; **Accepted:** 10 November, 2026

Abstract

Background: The epidermal growth factor receptor (EGFR) plays an important role in cell proliferation, survival, and tumor progression and is an established target for anticancer drug development. Quinazolinone derivatives have attracted interest as potential anticancer compounds.

Objectives: This study aimed to synthesize quinazolinone-based thioacetamide derivatives (3a–3k), evaluate their cytotoxicity against cancer and normal cells, and explore their potential interactions with epidermal growth factor receptor (EGFR) using molecular docking.

Methods: Compounds 3a–3k were synthesized through preparation of a mercaptoquinazolinone intermediate, synthesis of N-substituted 2-chloroacetamides, and subsequent S-alkylation. The compounds were characterized by IR, NMR, and mass spectrometry. Cytotoxicity was evaluated using the MTT assay against MCF-7, HepG2, HT-29, and A549 cancer cells and normal human dermal fibroblasts (HDF). Molecular docking was performed using wild-type EGFR and the L858R/T790M and L858R/T790M/C797S mutant structures (PDB IDs: 1M17, 4I22, and 6LUD), with erlotinib, gefitinib, osimertinib, and olmutinib included as reference ligands.

Results: Compounds 3b and 3d exhibited the most favorable overall cytotoxic profiles among the synthesized derivatives. Compound 3d showed IC_{50} values of 9.97, 13.93, 22.63, and 27.02 µM against MCF-7, HepG2, HT-29, and A549 cells, respectively, whereas the corresponding values for 3b were 10.72, 14.99, 20.15, and 27.24 µM. Both compounds were most active against MCF-7 cells, with selectivity indices relative to HDF cells of 4.23 for 3d and 3.74 for 3b. Molecular docking predicted plausible binding poses within the EGFR ATP-binding region. In the L858R/T790M/C797S model, compounds 3b and 3d yielded more negative docking scores than olmutinib, whereas 3k showed a comparable score.

Conclusions: Quinazolinone-based thioacetamide derivatives, particularly 3b and 3d, demonstrated promising in vitro cytotoxic activity, especially against MCF-7 cells, with some selectivity relative to HDF cells. Molecular docking suggested potential noncovalent interactions with EGFR; however, biochemical and cellular mechanistic studies are required to determine whether EGFR inhibition contributes to the observed cytotoxic effects.

Keywords: Quinazolinones, Thioacetamide, ErbB Receptors, Tyrosine Kinase Inhibitors, Molecular Docking Simulation, Antineoplastic Agents, Tetrazolium Salts

1. Introduction

Cancer remains a major global health challenge despite advances in diagnosis and treatment. Dysregulation of cellular proliferation, survival, and metastatic processes underscores the importance of identifying molecular targets and developing new anticancer agents. Among various malignancies, breast cancer is one of the most common cancers in women, and its molecular heterogeneity continues to necessitate the development of effective therapeutic strategies (1-3). The epidermal growth factor receptor (EGFR), also known as HER1 or ErbB1, is a receptor tyrosine kinase of the ErbB family that plays an important role in cancer progression. Ligand binding activates EGFR and stimulates downstream signaling pathways, including the RAS/RAF/MEK/ERK and PI3K/AKT/mTOR cascades, which regulate tumor-associated processes such as proliferation, survival, migration, and invasion. EGFR dysregulation, including overexpression and aberrant activation, has been reported in several solid

Copyright © 2026, Mansouri et al. This open-access article is available under the Creative Commons Attribution 4.0 (CC BY 4.0) International License (https://creativecommons.org/licenses/by/4.0/), which allows for unrestricted use, distribution, and reproduction in any medium, provided that the original work is properly cited.

How to Cite: Mansouri S, Salehi Ashani R, Tabatabai SA, Kobarfard F, Rezaee E, et al. Design, Synthesis, Cytotoxic Evaluation, and Molecular Docking Studies of Quinazolinone-Based Thioacetamide Derivatives as Potential Anticancer Agents. Iran J Pharm Res. 2026;25(1):e175904. doi: https://doi.org/10.5812/ijpr-175904

tumors, including breast, lung, and colorectal cancers, supporting its importance as a molecular target in anticancer drug discovery (1, 2, 4, 5). Accordingly, cancer cell lines derived from breast (MCF-7), hepatocellular (HepG2), colorectal (HT-29), and lung (A549) tissues were selected for the present study to evaluate the antiproliferative activity of the synthesized derivatives across tumor types in which EGFR dysregulation has been implicated. The therapeutic importance of EGFR has led to the development of several generations of EGFR tyrosine kinase inhibitors (EGFR-TKIs). Erlotinib is a representative first-generation EGFR-TKI, afatinib is a second-generation inhibitor, and olmutinib is a third-generation EGFR-TKI (Figure 1). These agents target the intracellular kinase domain of EGFR and inhibit receptor signaling through interactions with the ATP-binding region (6-8). Although EGFR-TKIs have demonstrated clinical benefits in selected tumors with activating EGFR alterations, particularly in subsets of non-small-cell lung cancer (NSCLC), acquired resistance remains a major limitation. Resistance-associated alterations, including T790M and C797S mutations, can reduce the efficacy of ATP-competitive EGFR inhibitors, emphasizing the need for novel chemical scaffolds capable of favorable interactions with distinct forms of EGFR (9-11).

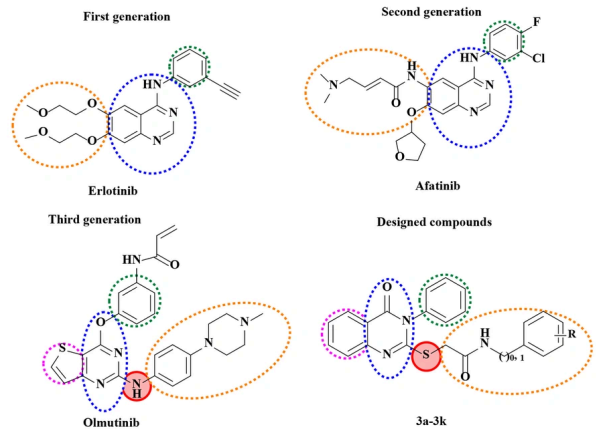


Figure 1. Structural comparison of first-, second-, and third-generation EGFR tyrosine kinase inhibitors (erlotinib, afatinib, and olmutinib, respectively) and the designed quinazolinone-based thioacetamide derivatives.

As illustrated in Figure 1, first-generation EGFR-TKIs, represented by erlotinib, contain a quinazoline core linked through an anilino NH linkage to a substituted aromatic ring bearing an ethynyl group that contributes to interactions within the EGFR kinase domain. The quinazoline core is further substituted with two 2-methoxyethoxy side chains. Second-generation inhibitors, such as afatinib, retain the quinazoline–anilino scaffold but were developed with an additional electrophilic acrylamide-type side chain that enables irreversible covalent interaction with Cys797. Third-generation EGFR-TKIs, exemplified by olmutinib, were designed to achieve improved selectivity toward mutant EGFR forms, particularly T790M, while minimizing inhibition of wild-type EGFR. Structurally, olmutinib features a thiophene ring fused to a pyrimidinone-type bicyclic core, an anilino NH linkage connecting this core to an N-methylpiperazinyl-phenyl moiety, and a separate phenyl ring bearing an acrylamide warhead responsible for covalent Cys797 binding.

Inspired by the structural characteristics of third-generation EGFR-TKIs, the present study applied a bioisosteric design strategy to this scaffold. The fused thiophene ring was replaced by a fused phenyl ring, converting the core into a genuine quinazolin-4(3H)-one scaffold; the anilino NH linkage was replaced by a sulfur atom; the acrylamide-bearing phenyl warhead was replaced by an unsubstituted phenyl ring, thereby eliminating the covalent electrophilic component; and the N-methylpiperazinyl-phenyl chain was replaced by a thioacetamide linker terminating in a phenyl or benzyl group bearing a variable substituent (R). These structural modifications were introduced to generate novel derivatives with features resembling those of third-generation EGFR-targeting agents and to investigate their potential anticancer activity and predicted interactions with EGFR.

From a medicinal chemistry perspective, heterocyclic scaffolds play an important role in developing biologically active compounds because of their structural diversity and ability to establish favorable interactions with biological targets. Among these scaffolds, quinazolin-4(3H)-one (quinazolinone) has attracted considerable attention because of its diverse pharmacological activities, particularly its reported antiproliferative and antitumor properties (12-17). Structural modification of the quinazolinone core can significantly influence the physicochemical properties and biological activity of the resulting derivatives. Quinazolinone-based compounds have been investigated as potential anticancer agents and as modulators of cancer-related targets, including EGFR (12-17). Previous structure–activity relationship studies, including the work of Sonousi et al., have demonstrated that modifications to the quinazolinone scaffold can affect antiproliferative activity and molecular interactions, supporting further exploration of this scaffold in anticancer drug discovery (18).

In addition to modifying the heterocyclic core, incorporating appropriate linkers is an effective strategy for modulating the biological properties of drug-like molecules. Previous studies have indicated that sulfur-containing linkers, including thioacetyl/thioacetamide groups, may influence the antiproliferative activity and molecular interactions of quinazolinone derivatives. Sonousi et al. reported quinazolinone derivatives bearing a thioacetyl bridge and suggested that linker modification could contribute to differences in biological activity (18). Therefore, incorporating sulfur-containing spacers into quinazolinone-based structures may provide a useful approach for generating new anticancer candidates.

2. Objectives

Based on these considerations, the present study was designed to synthesize a series of quinazolinone-based thioacetamide derivatives (3a–3k) and evaluate their in vitro cytotoxic activity against the MCF-7, HepG2, HT-29, and A549 cancer cell lines, as well as the normal human dermal fibroblast (HDF) cell line, using the MTT assay. The synthesized compounds were characterized by IR, NMR, and MS. Given their structural relationship to olmutinib, molecular docking studies were also performed to investigate their predicted binding modes and potential interactions within the EGFR binding site. Because no biochemical EGFR inhibition assay was performed, the docking findings were regarded as supportive computational evidence of a potential EGFR interaction rather than experimental confirmation of direct EGFR inhibition. Overall, this study provides insight into how structural modifications affect the antiproliferative activity of quinazolinone-based thioacetamide derivatives and identifies compounds with promising biological profiles for further structural optimization and mechanistic investigation.

3. Methods

3.1. Chemistry

3.1.1. General Materials and Methods

All chemicals and solvents used in this study were obtained from commercial suppliers and, when necessary, were used without further purification. The progress of the chemical reactions was monitored by thin-layer chromatography (TLC). The ^{1}H-NMR and ^{13}C-NMR spectra of the synthesized compounds were recorded using a Bruker spectrometer at 400 and 100 MHz, respectively, with DMSO-d^{6} as the solvent. Chemical shifts were reported as δ values in parts per million (ppm). Mass spectra were obtained using a FINNIGAN-MAT 8430 mass spectrometer. Melting points were measured using an Electrothermal 9100 melting point apparatus and are uncorrected. Spectroscopic data, melting points, and other physicochemical properties were used to confirm the structures of the synthesized products.

3.1.2. Synthesis of 2-Mercapto-3-phenylquinazolin-4(3H)-one (1)

Anthranilic acid (0.03 mol) and phenyl isothiocyanate (0.03 mol) were dissolved in 60 mL of absolute ethanol, and triethylamine (3 mL) was added. The reaction mixture was refluxed for 3 h. After completion of the reaction, the mixture was cooled to room temperature, and cold water and ice were added. The resulting mixture was stirred at room temperature for 15 min, and the precipitated solid was collected by filtration. The crude product was recrystallized from methanol to afford compound 1, which was subsequently used in the next synthetic step (19).

3.1.3. Synthesis of N-Substituted 2-Chloroacetamide Intermediates (2a–2k)

The appropriate benzylamine or aniline derivative (0.02 mol) was dissolved in THF (20 mL), treated with K_2CO_3 (0.02 mol), and stirred at room temperature for 30 min. A solution of chloroacetyl chloride (0.04 mol) in a small volume of THF was then added dropwise under ice-bath cooling in a fume hood, and the reaction mixture was heated under reflux for 24 h. Upon completion of the reaction, the solvent was evaporated under reduced pressure. The residue was diluted with distilled water (40 mL) and stirred for 20 min. The resulting solid was collected by filtration, washed with diethyl ether or petroleum ether, and, when necessary, further purified by recrystallization from methanol. The synthesized intermediates were monitored by thin-layer chromatography (TLC) and used directly in the next synthetic step.

3.1.4. Synthesis of Compounds (3a–3k)

For the synthesis of the final derivatives, 2-mercapto-3-phenylquinazolin-4(3H)-one (1, 0.0025 mol) was dissolved in methanol (20 mL). Separately, KOH (0.0025 mol) was dissolved in a small volume of methanol and added to the solution of compound 1. The resulting mixture was stirred at 60 °C in an oil bath for 30 min. The appropriate N-substituted 2-chloroacetamide intermediate (2a–2k, 0.0026 mol) was dissolved in a small volume of methanol and then added to the reaction mixture, which was heated under reflux for 12 h. Upon completion of the reaction, the mixture was cooled to room temperature, and water was

added. The precipitated solid was collected by filtration and dried. Product purity was monitored by TLC. When necessary, the crude products were washed with methanol or ethyl acetate to remove residual impurities and recrystallized from an appropriate solvent to afford the final derivatives 3a–3k.

2-(3,4-dihydro-4-oxo-3-phenylquinazolin-2-ylthio)-N-phenylacetamide (3a)

Molecular formula: $C_{22}H_{17}N_3O_2S$; molecular weight: 387.01 g/mol; isolated yield: 45%; white powder; melting point: 192 – 194 °C; MS: m/z 426 $[M + K]^+$; IR (KBr) υmax (cm^{-1}): 3294 (NH), 1684, 1654 (C=O); ^{1}H-NMR (400 MHz, DMSO-d_6) δ 4.94 (s, 2H, SCH_2), 7.05 (t, 1H, J = 7.2 Hz, H_4-phenyl), 7.31 (t, 2H, J = 8.0 Hz, H_3/H_5-phenyl), 7.21 – 7.26 (m, 3H, $H_2/H_4/H_6$-N_3-phenyl), 7.46 – 7.61 (m, 6H, H_3/H_5-N_3-phenyl, H_2/H_6-phenyl, H_6/H_8-quinazolinone), 7.84 (td, 1H, J = 6.8, 1.6 Hz, H_7-quinazolinone), 8.09 (dd, 1H, J = 6.8, 1.2 Hz, H_5-quinazolinone), 10.37 (s, 1H, NH); ^{13}C-NMR (100 MHz, DMSO-d_6) δ 37.78, 119.56 (2C), 120.02, 123.90, 126.38, 126.52, 127.10 (2C), 129.27 (2C), 129.91 (2C), 130.04, 130.49, 135.44, 136.26, 139.42, 147.61, 157.46, 161.11, 166.20.

2-(3,4-dihydro-4-oxo-3-phenylquinazolin-2-ylthio)-N-(4-methylphenyl)acetamide (3b)

Molecular formula: $C_{23}H_{19}N_3O_2S$; molecular weight: 401.12 g/mol; isolated yield: 76%; white powder; melting point: 225 – 227 °C; MS: m/z 402.1 $[M + H]^+$, 424 $[M + Na]^+$, 440 $[M + K]^+$; IR (KBr) υmax (cm^{-1}): 3294 (NH), 1684, 1662 (C=O); ^{1}H-NMR (400 MHz, DMSO-d_6) δ 2.24 (s, 3H, CH_3), 4.07 (s, 2H, SCH_2), 7.12 (d, 2H, J = 8.0 Hz, H_3/H_5-4-methylphenyl), 7.45 – 7.63 (m, 9H, $H_2/H_3/H_4/H_5/H_6$-N_3-phenyl, H_2/H_6-4-methylphenyl, H_6/H_8-quinazolinone), 7.83 (td, 1H, J = 7.2, 1.2 Hz, H_7-quinazolinone), 8.07 (dd, 1H, J = 7.6, 0.8 Hz, H_5-quinazolinone), 10.28 (s, 1H, NH); ^{13}C-NMR (100 MHz, DMSO-d_6) δ 20.91, 37.77, 119.56 (2C), 120.02, 126.38, 126.50, 127.09 (2C), 129.64 (2C), 129.91 (2C), 130.03, 130.48, 132.81, 135.43, 136.27, 136.93, 147.62, 157.48, 161.11, 165.91.

2-(3,4-dihydro-4-oxo-3-phenylquinazolin-2-ylthio)-N-(4-methoxyphenyl)acetamide (3c)

Molecular formula: $C_{23}H_{19}N_3O_3S$; molecular weight: 417.11 g/mol; isolated yield: 81%; white powder; melting point: 193 – 195 °C; MS: m/z 418 $[M + H]^+$, 440 $[M + Na]^+$, 456 $[M + K]^+$, 857 $[2M + Na]^+$, 873.1 $[2M + K]^+$; IR (KBr) υmax (cm^{-1}): 3272 (NH), 1695, 1651 (C=O); ^{1}H-NMR (400 MHz, DMSO-d_6) δ 3.71 (s, 3H, OCH_3), 4.06 (s, 2H, SCH_2), 6.89 (d, 2H, J = 9.2 Hz, H_3/H_5-4-methoxyphenyl), 7.45 – 7.62 (m, 9H, $H_2/H_3/H_4/H_5/H_6$-N_3-phenyl, H_2/H_6-4-methoxyphenyl, H_6/H_8-quinazolinone), 7.83 (td, 1H, J = 6.8, 1.2 Hz, H_7-quinazolinone), 8.07 (dd, 1H, J = 6.8, 1.2 Hz, H_5-quinazolinone), 10.23 (s, 1H, NH); ^{13}C NMR (100 MHz, DMSO-d_6) δ 37.70, 55.61, 114.36, 120.02, 121.13 (2C), 126.39, 126.50, 127.09, 129.91 (2C), 130.03 (2C), 130.48 (2C), 132.56, 135.43, 136.27, 147.63, 155.78, 157.48, 161.12, 165.63.

2-(3,4-dihydro-4-oxo-3-phenylquinazolin-2-ylthio)-N-(4-chlorophenyl)acetamide (3d)

Molecular formula: $C_{22}H_{16}ClN_3O_2S$; molecular weight: 421.07 g/mol; isolated yield: 65%; white powder; melting point: 233 – 235 °C; MS: m/z 422 $[M + H]^+$; IR (KBr) υmax (cm^{-1}): 3343 (NH), 1695, 1666 (C=O); ^{1}H-NMR (400 MHz, DMSO-d_6) δ 4.08 (s, 2H, SCH_2), 7.38 (d, 2H, J = 8.8 Hz, H_3/H_5-4-chlorophenyl), 7.45 – 7.64 (m, 9H, $H_2/H_3/H_4/H_5/H_6$-N_3-phenyl, H_2/H_6-4-chlorophenyl, H_6/H_8-quinazolinone), 7.84 (td, 1H, J = 6.8, 1.2 Hz, H_7-quinazolinone), 8.08 (dd, 1H, J = 6.8, 1.2 Hz, H_5-quinazolinone), 10.52 (s, 1H, NH); ^{13}C-NMR (100 MHz, DMSO-d_6) δ 37.73, 120.03, 121.08 (2C), 126.35 (2C), 126.52, 127.10, 127.42, 129.20 (2C), 129.90 (2C), 130.04, 130.50, 135.44, 136.25, 138.39, 147.59, 157.40, 161.09, 166.43.

2-(3,4-dihydro-4-oxo-3-phenylquinazolin-2-ylthio)-N-(4-fluorophenyl)acetamide (3e)

Molecular formula: $C_{22}H_{16}FN_3O_2S$; molecular weight: 405.09 g/mol; isolated yield: 71%; white powder; melting point: 171 – 174 °C; MS: m/z 406 $[M + H]^+$, 428 $[M + Na]^+$, 444 $[M + K]^+$; IR (KBr) υmax (cm^{-1}): 3339 (NH), 1695, 1669 (C=O); ^{1}H-NMR (400 MHz, DMSO-d_6) δ 4.08 (s, 2H, SCH_2), 7.18 (t, 2H, J = 8.8 Hz, H_3/H_5-4-fluorophenyl), 7.45 – 7.63 (m, 9H, $H_2/H_3/H_4/H_5/H_6$-N_3-phenyl, H_2/H_6-4-fluorophenyl, H_6/H_8-quinazolinone), 7.84 (td, 1H, J = 6.8, 1.6 Hz, H_7-quinazolinone), 8.09 (dd, 1H, J = 6.8, 0.8 Hz, H_5-quinazolinone), 10.43 (s, 1H, NH); ^{13}C-NMR (100 MHz, DMSO-d_6) δ 37.68, 115.74, 115.96, 120.03, 121.29, 127.37, 126.37, 126.51, 127.10, 129.91, 130.04, 130.49, 135.43, 135.81, 135.84, 136.26, 147.61, 157.33, 157.43, 159.71, 161.10, 166.14.

2-(3,4-dihydro-4-oxo-3-phenylquinazolin-2-ylthio)-N-(3,4-dichlorophenyl)acetamide (3f)

Molecular formula: $C_{22}H_{15}C_{l2}N_3O_2S$; molecular weight: 455.03 g/mol; isolated yield: 50%; white powder; melting point: 227 – 230 °C; MS: m/z 456 $[M + H]^+$; IR (KBr) υmax (cm^{-1}): 3313 (NH), 1681, 1670 (C=O); ^{1}H-NMR (400 MHz, DMSO-d_6) δ 4.01 (s, 2H, SCH_2), 7.45 (td, 1H, J = 8.0, 1.2 Hz, H_4-N_3-phenyl), 7.49 – 7.63 (m, 8H, $H_2/H_3/H_5/H_6$-N_3-phenyl, H_5/H_6-3,4-dichlorophenyl, H_6/H_8-quinazolinone), 7.83 (td,

1H, J = 6.8, 1.2 Hz, H_7-quinazolinone), 8.00 (d, 1H, J = 2.4 Hz, H_2-3,4-dichlorophenyl), 8.08 (dd, 1H, J = 6.8, 1.2 Hz, H_5-quinazolinone), 10.69 (s, 1H, NH); ^{13}C-NMR (100 MHz, DMSO-d_6) δ 37.72, 119.56, 120.02, 120.71(2C), 125.32, 126.33, 126.52, 127.10, 129.90(2C), 130.04, 130.51, 131.24, 131.54, 135.42, 136.23, 139.51, 147.56, 157.32, 161.08, 166.89.

2-(3,4-dihydro-4-oxo-3-phenylquinazolin-2-ylthio)-N-benzylacetamide (3g)

Molecular formula: $C_{23}H_{19}N_3O_2S$; molecular weight: 401.12 g/mol; isolated yield: 50%; white powder; melting point: 190 – 193 °C; MS: m/z 402.1 $[M + H]^+$, 424.1 $[M + Na]^+$, 440.1 $[M + K]^+$; IR (KBr) υmax (cm^{-1}): 3283 (NH), 1692, 1643 (C=O); ^{1}H-NMR (400 MHz, DMSO-d_6) δ 3.95 (s, 2H, SCH_2), 4.31 (d, 2H, J = 5.6 Hz, CH_2-benzyl), 7.21 – 7.26 (m, 5H, H_2/H_3/H_4/H_5/H_6-benzyl), 7.47 – 7.61 (m, 7H, H_2/H_3/H_4/H_5/H_6-N_3-phenyl, H_6/H_8-quinazolinone), 7.87 (td, 1H, J = 6.8, 1.6 Hz, H_7-quinazolinone), 8.09 (dd, 1H, J = 6.8, 0.8 Hz, H_5-quinazolinone), 8.72 (t, 1H, J = 5.6 Hz, NH). ^{13}C-NMR (100 MHz, DMSO-d_6) δ 36.46, 42.92, 120.00 (2C), 126.49, 126.56, 127.03 (2C), 127.20, 127.27, 127.51, 128.67, 129.91 (2C), 130.00, 130.44, 135.35, 136.28, 139.62, 147.62, 157.41, 161.17, 167.20.

2-(3,4-dihydro-4-oxo-3-phenylquinazolin-2-ylthio)-N-(4-methylbenzyl)acetamide (3h)

Molecular formula: $C_{24}H_{21}N_3O_2S$; molecular weight: 415.14 g/mol; isolated yield: 86%; white powder; melting point: 194 – 197 °C; MS: m/z 416.2 $[M + H]^+$, 438.2 $[M + Na]^+$, 454.2 $[M + K]^+$; IR (KBr) υmax (cm^{-1}): 3287 (NH), 1692, 1640 (C=O); ^{1}H-NMR (400 MHz, DMSO-d_6) δ 2.25 (s, 3H, CH_3-4-methylbenzyl), 3.93 (s, 2H, SCH_2), 4.25 (d, 2H, J = 6.0 Hz, CH_2-benzyl), 7.06 (d, 2H, J = 8.0 Hz, H_3/H_5-4-methylbenzyl), 7.14 (d, 2H, J = 8.0 Hz, H_2/H_6-4-methylbenzyl), 7.47 – 7.62 (m, 7H, H_2/H_3/H_4/H_5/H_6-N_3-phenyl, H_6/H_8-quinazolinone), 7.87 (td, 1H, J = 7.2, 1.2 Hz, H_7-quinazolinone), 8.09 (dd, 1H, J = 7.2, 1.6 Hz, H_5-quinazolinone), 8.68 (t, 1H, J = 6.0 Hz, NH). ^{13}C-NMR (100 MHz, DMSO-d_6) δ 21.15, 36.51, 42.70, 119.99, 126.48, 126.56, 127.01, 127.57, 127.69, 129.22 (2C), 129.90 (2C), 130.00 (2C), 130.43, 135.30, 136.24, 136.28, 136.56, 147.61, 157.39, 161.17, 167.10.

2-(3,4-dihydro-4-oxo-3-phenylquinazolin-2-ylthio)-N-(4-methoxybenzyl)acetamide (3i)

Molecular formula: $C_{24}H_{21}N_3O_3S$; molecular weight: 431.13 g/mol; isolated yield: 78%; white powder; melting point: 190 – 192 °C; MS: m/z 432 $[M + H]^+$, 454.1 $[M + Na]^+$, 470 $[M + K]^+$; IR (KBr) υmax (cm^{-1}): 3224 (NH), 1681, 1643 (C=O); ^{1}H-NMR (400 MHz, DMSO-d_6) δ 3.71 (s, 3H, OCH_3), 3.92 (s, 2H, SCH_2), 4.22 (d, 2H, J = 5.6 Hz, CH_2-benzyl), 6.82 (d, 2H, J = 8.4 Hz, H_3/H_5-4-methoxybenzyl), 7.18 (d, 2H, J = 8.8 Hz, H_2/H_6-4-methoxybenzyl), 7.47 – 7.62 (m, 7H, H_2/H_3/H_4/H_5/H_6-N_3-phenyl, H_6/H_8-quinazolinone), 7.83 (td, 1H, J = 7.2, 1.6 Hz, H_7-quinazolinone), 8.09 (dd, 1H, J = 7.2, 1.2 Hz, H_5-quinazolinone), 8.65 (t, 1H, J = 5.6 Hz, NH). ^{13}C-NMR (100 MHz, DMSO-d_6) δ 36.54, 42.41, 55.48, 114.05 (2C), 120.00, 126.47, 126.57, 127.01, 128.93 (2C), 129.91 (2C), 130.00 (2C), 130.43, 131.53, 135.29, 136.28, 147.60, 157.40, 158.62, 161.16, 167.02.

2-(3,4-dihydro-4-oxo-3-phenylquinazolin-2-ylthio)-N-(4-chlorobenzyl)acetamide (3j)

Molecular formula: $C_{23}H_{18}ClN_3O_2S$; molecular weight: 435.08 g/mol; isolated yield: 80%; white powder; melting point: 193 – 195 °C; MS: m/z 436 $[M + H]^+$, 458 $[M + Na]^+$, 474 $[M + K]^+$; IR (KBr) υmax (cm^{-1}): 3298 (NH), 1692, 1640 (C=O); ^{1}H-NMR (400 MHz, DMSO-d_6) δ 3.94 (s, 2H, SCH_2), 4.29 (d, 2H, J = 6.0 Hz, CH_2-benzyl), 7.31 – 7.61 (m, 4H, H_2/H_3/H_5/H_6-4-chlorobenzyl), 7.47 – 7.61 (m, 7H, H_2/H_3/H_4/H_5/H_6-N_3-phenyl, H_6/H_8-quinazolinone), 7.86 (td, 1H, J = 6.8, 1.6 Hz, H_7-quinazolinone), 8.10 (dd, 1H, J = 6.8, 0.8 Hz, H_5-quinazolinone), 8.70 (t, 1H, J = 6.0 Hz, NH). ^{13}C-NMR (100 MHz, DMSO-d_6) δ 36.44, 42.31, 120.01, 126.50, 126.52, 127.04, 128.59 (2C), 129.43 (2C), 129.91 (2C), 130.00 (2C), 130.44, 131.73, 135.30, 136.27, 138.76, 147.59, 157.37, 161.16, 167.33.

2-(3,4-dihydro-4-oxo-3-phenylquinazolin-2-ylthio)-N-(4-fluorobenzyl)acetamide (3k)

Molecular formula: $C_{23}H_{18}FN_3O_2S$; molecular weight: 419.11 g/mol; isolated yield: 58%; white powder; melting point: 210 – 212 °C; MS: m/z 420.1 $[M + H]^+$, 442 $[M + Na]^+$, 861 $[2M + Na]^+$; IR (KBr) υmax (cm^{-1}): 3287 (NH), 1695, 1643 (C=O); ^{1}H-NMR (400 MHz, DMSO-d_6) δ 3.93 (s, 2H, SCH_2), 4.28 (d, 2H, J = 5.6 Hz, CH_2-benzyl), 7.09 (t, 2H, J = 8.8 Hz, H_3/H_5-4-fluorobenzyl), 7.30 (dd, 2H, J = 9.2, 3.2 Hz, H_2/H_6-4-fluorobenzyl), 7.47 – 7.62 (m, 7H, H_2/H_3/H_4/H_5/H_6-N_3-phenyl, H_6/H_8-quinazolinone), 7.85 (td, 1H, J = 6.8, 1.2 Hz, H_7-quinazolinone), 8.09 (dd, 1H, J = 6.8, 1.2 Hz, H_5-quinazolinone), 8.72 (t, 1H, J = 5.6 Hz, NH). ^{13}C-NMR (100 MHz, DMSO-d_6) δ 36.46, 42.25, 115.27 (2C), 115.48, 120.00, 126.50, 127.03, 129.49, 129.57, 129.91, 130.00, 130.44, 135.33, 135.83, 135.86, 136.27, 147.60, 157.39, 160.38, 161.15, 162.78, 167.23.

3.2. Cytotoxic Activity of the Synthesized Compounds

The cytotoxic activity of compounds 3a–3k was evaluated using the MTT assay against four human cancer cell lines: MCF-7 (breast cancer), HepG2 (hepatocellular carcinoma), HT-29 (colorectal adenocarcinoma), and A549 (lung cancer), as well as normal human dermal fibroblasts

(HDF). Cells were obtained from the National Cell Bank of Iran (NCBI), Pasteur Institute of Iran, Tehran, Iran, and cultured in RPMI-1640 medium supplemented with 10% fetal bovine serum (FBS) and 1% penicillin/streptomycin at 37 °C in a humidified atmosphere containing 5% CO_2. Cells were seeded in 96-well plates at a density of 1×10^4 cells/well and allowed to attach for 24 h. The cells were then treated with the test compounds at concentrations of 1, 10, 25, 50, and 100 µM for 24 h. The compounds were dissolved in water/DMSO, with the final DMSO concentration maintained at ≤ 0.1% (v/v). Each concentration was tested in technical triplicate, and vehicle-treated wells served as controls. Doxorubicin was included as the reference cytotoxic agent. Following treatment, MTT solution (0.5 mg/mL) was added to each well, and the plates were incubated for 3 – 4 h at 37 °C. The resulting formazan crystals were dissolved in DMSO, and absorbance was measured at 570 nm. To evaluate potential assay interference, cell-free control wells containing the test compounds and MTT reagent were included to assess possible direct interactions with MTT and/or absorbance interference at 570 nm. Potential interference of the test compounds with the MTT assay was assessed under cell-free conditions. Data were analyzed using GraphPad Prism 10. Responses were normalized to the vehicle-treated controls, and IC_{50} values were estimated by nonlinear regression using a four-parameter logistic model (log[inhibitor] versus normalized response, variable slope). Each concentration was tested in three technical replicate wells within a single experiment (n = 3 wells per concentration). Accordingly, the reported IC_{50} values represent best-fit estimates obtained from these technical replicates and do not reflect variability across independent biological experiments. The corresponding 95% profile-likelihood confidence intervals (CIs) and goodness-of-fit values (R^2) are provided in Supplementary Table S1. These CIs reflect the uncertainty associated with the curve-fitting procedure and should not be interpreted as measures of between-experiment variability. The selectivity index (SI) was calculated as the ratio of the IC_{50} value in HDF cells to that in each respective cancer cell line (SI = IC_{50} [HDF]/IC_{50} [cancer cells]). Because the measurements were obtained from technical replicates within a single experiment, no inferential statistical tests were performed. Independent biological replicates will be required in future studies to assess experimental variability and statistical significance (20-22).

3.3. Molecular Docking Study

Molecular docking studies were performed to investigate the predicted binding poses and potential noncovalent interactions of the synthesized derivatives within the ATP-binding sites of three EGFR structures: wild-type EGFR (PDB ID: 1M17), the L858R/T790M mutant (PDB ID: 4I22), and the L858R/T790M/C797S mutant (PDB ID: 6LUD). These structures were selected to evaluate the predicted binding modes of the synthesized compounds in wild-type and drug-resistant EGFR models. Erlotinib, gefitinib, and osimertinib were used as reference ligands for 1M17, 4I22, and 6LUD, respectively. Olmutinib was also docked as an additional comparator because it was used as a design reference during the development of the synthesized derivatives. Thus, osimertinib served as the native co-crystallized reference ligand for 6LUD, whereas olmutinib was included for comparative analysis. The crystallographic structures were obtained from the Protein Data Bank (PDB). Before docking, the co-crystallized ligands were removed from the receptor structures, and nonessential molecules were removed as appropriate. Polar hydrogens and atomic charges were added during protein preparation using AutoDockTools (version 1.5.6.rc3). The ligands were prepared as three-dimensional structures suitable for docking calculations. Molecular docking was performed using AutoDock Vina. The docking search space for each EGFR structure was defined by a cubic grid box measuring 20 × 20 × 20 Å and centered on the coordinates of the corresponding co-crystallized ligand. The grid-box centers were as follows: 1M17, x = 22.0137, y = 0.2528, z = 52.7940; 4I22, x = 10.1998, y = −15.7625, z = 11.2116; and 6LUD, x = −49.7306, y = −0.0390, z = −18.2199. These coordinates were selected to encompass the ATP-binding region of each receptor. The exhaustiveness parameter was set to 100, and up to 50 docking poses were generated for each ligand–protein system (num_modes = 50). The docking protocol was validated by redocking each native co-crystallized ligand into its corresponding EGFR binding site using the same docking settings. The predicted redocked pose was compared with the experimentally observed crystallographic pose by calculating the root-mean-square deviation (RMSD). RMSD values were used to assess the ability of the docking protocol to reproduce the experimentally observed ligand poses. Docking poses were ranked according to their predicted docking scores (kcal/mol). The resulting protein–ligand complexes were visualized using molecular visualization software, and predicted hydrogen-bonding, hydrophobic, π-related, and other noncovalent interactions with residues in the binding pocket were examined. Residue numbering was standardized when comparing the EGFR structures; specifically, Met769 in 1M17 corresponds to Met793 under the numbering convention used for the other EGFR structures. The docking scores and predicted interactions were interpreted as computational estimates of potential binding modes and were not considered direct evidence of EGFR inhibition or ATP-competitive activity. Because no

biochemical EGFR inhibition assay or EGFR-dependent cellular assay was performed, further experimental studies are required to determine whether EGFR contributes to the observed cytotoxic effects.

4. Results and Discussion

4.1. Chemistry

As shown in Figure 2, the key intermediate 2-mercapto-3-phenylquinazolin-4(3H)-one (1) was synthesized via cyclocondensation of anthranilic acid with phenyl isothiocyanate in the presence of Et_3N under reflux in absolute ethanol for 3 h (step a). In parallel, a series of N-substituted 2-chloroacetamide intermediates (2a–2k) were prepared by reacting the appropriate amines with chloroacetyl chloride in the presence of K_2CO_3 in THF at room temperature for 30 min, followed by reflux for 24 h (step b). Finally, the target quinazolinone derivatives 3a–3k were obtained via S-alkylation of compound 1 with intermediates 2a–2k using KOH as the base in methanol under reflux for 12 h (step c).

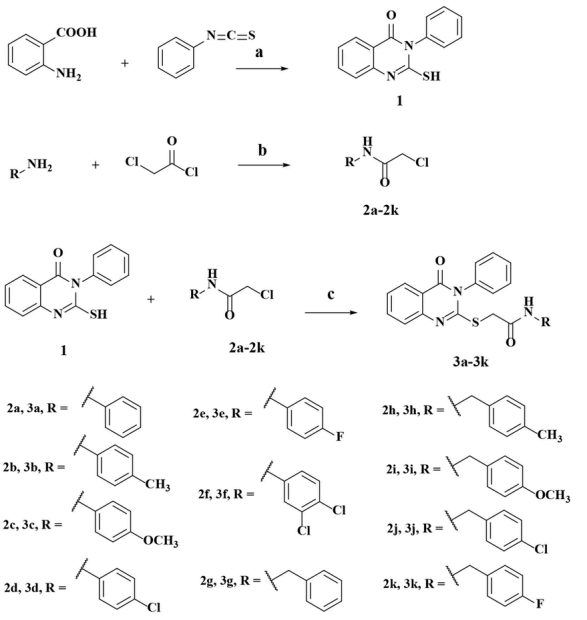
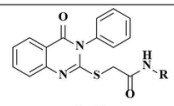


Figure 2. General synthetic methods. Reagents and conditions: (a) Et_3N, absolute ethanol, reflux, 3 h; (b) K_2CO_3, THF, rt, 30 min, then reflux, 24 h; (c) KOH, methanol, reflux, 12 h.

4.2. Cytotoxic Activity of the Synthesized Compounds

The cytotoxicity results revealed differences in the sensitivity of the four cancer cell lines to the synthesized compounds. The IC_{50} values of compounds 3a–3k and doxorubicin against MCF-7, HepG2, HT-29, and A549 cells, together with the corresponding selectivity indices (SIs), are summarized in Figure 3. Among the synthesized derivatives, 3d exhibited the greatest overall cytotoxic activity, with IC_{50} values of 9.97, 13.93, 22.63, and 27.02 µM against MCF-7, HepG2, HT-29, and A549 cells, respectively. Compound 3b showed a comparable profile, with corresponding IC_{50} values of 10.72, 14.99, 20.15, and 27.24 µM, and was the most active derivative against HT-29 cells. Both compounds showed their greatest activity against MCF-7 cells. Compound 3i also displayed activity against MCF-7 cells (IC_{50} = 12.85 µM) and was the most active N-benzyl derivative across the four cancer cell lines, although it was less potent than 3b and 3d. The remaining compounds generally exhibited lower cytotoxic activity, with potency varying across cell lines. For example, compound 3j showed IC_{50} values of 24.48, 31.14, 44.72, and 47.07 µM against MCF-7, HepG2, HT-29, and A549 cells, respectively. Overall, MCF-7 cells appeared to be the most sensitive cell line, followed by HepG2, whereas HT-29 and A549 cells generally showed lower sensitivity. As expected, doxorubicin was substantially more potent than the synthesized derivatives, with IC_{50} values ranging from 1.10 to 1.56 µM across the four cancer cell lines. Comparison of the cytotoxicity profiles suggested that aromatic substitution and linker type may influence the activity of these derivatives. Among the N-aryl compounds, the 4-methyl-substituted derivative 3b and the 4-chloro-substituted derivative 3d were more active than the unsubstituted analogue 3a across the four cancer cell lines. In contrast, the 4-methoxy-substituted derivative 3c showed lower activity than 3a, whereas the 3,4-dichloro-substituted derivative 3f was less active than the 4-chloro analogue 3d. Within the N-benzyl series, the 4-methoxy-substituted derivative 3i showed the greatest cytotoxic activity, suggesting that the influence of a substituent may depend on whether the aromatic ring is attached directly to the amide nitrogen or separated from it by a methylene group. These observations suggest preliminary structure–activity relationship (SAR) trends; however, further studies involving a broader range of derivatives are required to establish these relationships more conclusively. Although previous studies have reported anticancer activity among quinazolinone derivatives (18, 23), the cytotoxic effects observed in the present study do not establish EGFR inhibition as the underlying mechanism. The findings should also be interpreted in light of the limitations of the experimental design. The use of a single non-malignant cell model (human dermal fibroblasts [HDF]) and a 24-h exposure period provides an initial assessment of



3a-3k

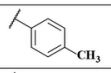
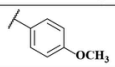
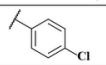
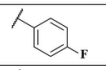
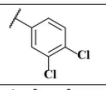
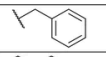
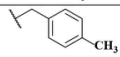
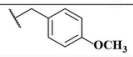
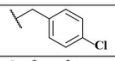
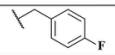
NO	R	MCF-7		HepG2		HT-29		A549		HDF
		IC_{50} (μM)	SI*	IC_{50} (μM)	SI*	IC_{50} (μM)	SI*	IC_{50} (μM)	SI*	IC_{50} (μM)
3a		13.23	3.48	23.02	2.00	34.90	1.32	38.75	1.19	46.00
3b		10.72	3.74	14.99	2.68	20.15	1.99	27.24	1.47	40.10
3c		30.61	1.90	38.46	1.51	41.80	1.39	54.98	1.06	58.21
3d		9.97	4.23	13.93	3.03	22.63	1.86	27.02	1.56	42.15
3e		27.25	2.04	36.01	1.54	27.37	2.03	42.57	1.31	55.60
3f		25.21	2.52	33.27	1.91	30.26	2.10	50.03	1.27	63.50
3g		29.65	1.95	35.81	1.62	37.30	1.55	44.56	1.30	57.89
3h		20.56	2.21	28.28	1.61	32.15	1.41	38.02	1.20	45.49
3i		12.85	3.35	22.11	1.95	26.03	1.65	32.78	1.31	43.05
3j		24.48	2.88	31.14	2.27	44.72	1.58	47.07	1.50	70.55
3k		24.39	2.31	32.28	1.74	33.86	1.66	43.83	1.28	56.30
Doxorubicin		1.10	7.92	1.45	6.01	1.44	6.05	1.56	5.58	8.71

Figure 3. IC_{50} values of the synthesized compounds 3a–3k and doxorubicin against cancer and normal HDF cell lines, together with the corresponding selectivity indices. * Selectivity Index (SI) was calculated as SI = IC_{50} (HDF, μM) / IC_{50} (cancer cell line, μM); higher SI values indicate greater selectivity toward the corresponding cancer cell line relative to normal human dermal fibroblast (HDF) cells.

cytotoxicity but is insufficient to establish general safety or definitive tumor selectivity (20-22). Furthermore, the selectivity indices indicate relative differences in sensitivity between cancer cells and HDF cells rather than demonstrating a therapeutic window. Future studies using additional non-malignant cell models and longer exposure periods (e.g., 48 and 72 h) would help further characterize the cytotoxic profiles of these compounds. To assess the relative selectivity of the synthesized compounds for cancer cells over normal HDF cells, the selectivity index (SI) was calculated (Figure 3). Higher SI values indicate a greater difference between the concentrations required to reduce cancer-cell and HDF-cell viability. Compound 3d showed the highest SI values against MCF-7 and HepG2 cells (4.23 and 3.03, respectively), followed by 3b (3.74 and 2.68, respectively). Against HT-29 cells, 3f exhibited the highest SI (2.10), followed by 3e (2.03) and 3b (1.99). In comparison, 3d had an SI of 1.86 against HT-29 cells, indicating that cytotoxic potency and relative selectivity varied by cell line. Overall, SI values were generally higher for MCF-7 cells and lower for A549 cells. Doxorubicin exhibited higher SI values than all synthesized derivatives across the four cancer cell lines.

Taken together, 3b and 3d displayed the most favorable overall cytotoxic profiles within the series, particularly against MCF-7 and HepG2 cells. However, their SI values indicate moderate relative selectivity, and both compounds were substantially less potent than doxorubicin. Accordingly, these derivatives should be considered candidates for further structural optimization

and biological evaluation rather than established selective anticancer agents. Because the MTT assay measures cellular metabolic activity but does not identify the molecular mechanism responsible for the observed effects, molecular docking was performed to explore the potential interactions of the synthesized compounds with EGFR. The docking results provide computational predictions of possible binding modes but do not establish direct EGFR inhibition or an ATP-competitive mechanism. Biochemical EGFR kinase assays and appropriate cellular studies will be required to determine whether EGFR contributes to the observed cytotoxic activity.

4.3. Molecular Docking Results

To explore the potential interactions of the synthesized derivatives with the epidermal growth factor receptor (EGFR) and characterize th

eir predicted binding modes within the ATP-binding region, molecular docking studies were performed using three crystallographic EGFR structures: wild-type EGFR (PDB ID: 1M17), the L858R/T790M double mutant (PDB ID: 4I22), and the L858R/T790M/C797S triple mutant (PDB ID: 6LUD). These structures represent distinct EGFR molecular backgrounds, including mutations associated with resistance to EGFR tyrosine kinase inhibitors. The T790M and C797S substitutions are particularly relevant to inhibitor sensitivity and have motivated investigations into alternative approaches for targeting mutant EGFR (9-11, 24, 25). The C797S substitution is of particular interest because Cys797 serves as the covalent binding site for several irreversible EGFR inhibitors. As the synthesized compounds lack an electrophilic warhead designed to form a covalent bond with Cys797, their predicted interactions are expected to rely primarily on noncovalent contacts within the ATP-binding region (10, 24-26). The docking protocol was validated separately for each EGFR structure by re-docking its respective co-crystallized ligand into the corresponding binding site. The calculated RMSD values between the re-docked and crystallographic ligand poses were 0.255 Å for erlotinib (1M17), 0.170 Å for gefitinib (4I22), and 0.947 Å for osimertinib (6LUD). All RMSD values were below the commonly accepted threshold of 2.0 Å, indicating good reproduction of the experimentally observed ligand poses and supporting the suitability of the docking protocol for the subsequent analyses. Images illustrating the superposition of the re-docked and crystallographic ligand poses are provided in the Supplementary Materials. Images of the re-docking results are provided in the Supplementary Materials. Erlotinib, gefitinib, and osimertinib were used as reference ligands for the 1M17, 4I22, and 6LUD structures, respectively. Olmutinib was additionally included as a comparator because it informed the design of the synthesized derivatives. The docking scores and predicted ligand–protein interactions are summarized in Table 1. More negative docking scores indicate more favorable predicted poses according to the applied computational protocol; however, these scores should not be interpreted as experimentally determined binding free energies. For wild-type EGFR (1M17), all synthesized compounds yielded more negative docking scores than erlotinib (−7.2 kcal/mol). Compound 3e produced the most negative score (−10.3 kcal/mol), followed by 3c (−10.0 kcal/mol) and 3h and 3j (−9.9 kcal/mol each). Compound 3k had the least negative score among the derivatives (−8.9 kcal/mol), which was still more negative than that of erlotinib. Similarly, in the L858R/T790M mutant model (4I22), all derivatives yielded more negative scores than gefitinib (−8.7 kcal/mol). Compound 3a showed the most negative score (−10.4 kcal/mol), followed by 3b and 3e (−10.2 kcal/mol each) and 3d and 3h (−10.0 kcal/mol each); the other derivatives had scores ranging from −9.1 to −9.9 kcal/mol. For the L858R/T790M/C797S mutant model (6LUD), compound 3b yielded the most negative docking score (−9.0 kcal/mol), followed by 3d (−8.7 kcal/mol). Compound 3k had a score of −8.6 kcal/mol, equal to the reported score for osimertinib and more negative than that of olmutinib (−8.5 kcal/mol). Compounds 3h and 3j also had scores of −8.5 kcal/mol, comparable to olmutinib, whereas the remaining derivatives showed less negative scores. These results suggest that several derivatives may adopt favorable predicted poses within the modeled EGFR ATP-binding regions. Nevertheless, docking results alone cannot establish direct EGFR inhibition, cellular target engagement, or an ATP-competitive mechanism. Comparison across the three EGFR models indicated that the relationship between terminal aromatic substitution and docking score depended on the modeled receptor structure. Within the N-aryl series, the para-methyl derivative 3b and the para-chloro derivative 3d yielded relatively favorable scores against the mutant models. In 6LUD, their scores (−9.0 and −8.7 kcal/mol, respectively) were more negative than that of the unsubstituted analogue 3a (−8.3 kcal/mol). By contrast, the para-methoxy derivative 3c and para-fluoro derivative 3e yielded scores of −8.3 kcal/mol each against 6LUD, while additional chlorination in 3f (3,4-dichloro substitution) did not improve the score relative to 3d. These observations are consistent with the possibility that substituent size, lipophilicity, and electronic properties influence the predicted binding poses; however, the docking results do not establish a definitive structure–activity relationship or a specific binding mechanism. The N-benzyl derivatives (3g–3k) contain an additional methylene spacer that may affect conformational flexibility and the orientation of the

terminal aromatic ring. The docking scores varied across the three EGFR receptor models, and no single compound consistently achieved the most favorable score in all three models. Therefore, the docking results do not support a general conclusion that one derivative or substitution pattern is superior across the different EGFR structures. Instead, the findings provide a basis for further investigation of these compounds.

Table 1. Predicted Molecular Docking Scores of 3a–3k Against Different EGFR Structures [a]

Compound	EGFR (1M17) Wild-Type	EGFR (4I22) L858R/T790M	EGFR (6LUD) L858R/T790M/C797S
3a	−9.8	−10.4	−8.3
3b	−9.6	−10.2	−9.0
3c	−10.0	−9.5	−8.3
3d	−9.5	−10.0	−8.7
3e	−10.3	−10.2	−8.3
3f	−9.4	−9.4	−8.2
3g	−9.7	−9.6	−8.0
3h	−9.9	−10.0	−8.5
3i	−9.6	−9.1	−8.4
3j	−9.9	−9.9	−8.5
3k	−8.9	−9.6	−8.6
Erlotinib	−7.2	-	-
Gefitinib	-	−8.7	-
Olmutinib	-	-	−8.5
Osimertinib	-	-	−8.6

[a] Values are predicted docking scores (kcal/mol); more negative scores indicate more favorable predicted poses. Abbreviation: EGFR, epidermal growth factor receptor.

Based on their cytotoxic profiles and docking scores, compounds 3b and 3d were selected for further analysis of their predicted interactions with the three EGFR models. The docking poses suggested that both compounds could be accommodated within the modeled ATP-binding region; however, the predicted interactions differed among the receptor structures. In the 1M17 structure, both compounds were predicted to occupy the ATP-binding pocket in a manner similar to erlotinib. Both 3b and 3d formed a hydrogen bond with Thr766, together with an electrostatic π–cation interaction with Lys721. Additional hydrophobic and π-related interactions with Val702, Leu820, and Ala719 contributed to ligand stabilization, and in 3d the chlorine substituent further contacted Leu694 (Figure 4). In comparison, erlotinib formed a hydrogen bond with Lys721 and hydrophobic/π-related interactions with Phe859, Val702, Leu820, and Ala719, thus engaging several of the same residues as the designed compounds.

Further examination of the three-dimensional docking poses revealed differences in ligand proximity to the hinge-region residue Met769. Erlotinib was located approximately 4.8 Å from Met769, whereas compounds 3b and 3d were located 5.51 and 5.54 Å from this residue, respectively (Supplementary Figure S4). These distances indicate that 3b and 3d are not favorably positioned to form a direct hydrogen bond with Met769 in the wild-type EGFR model. The proximity of erlotinib to Met769 does not, by itself, establish hydrogen-bond formation, which also depends on the interaction geometry. These interaction patterns suggest that the quinazolinone–thioacetamide scaffold can be accommodated within the modeled wild-type EGFR ATP-binding pocket through a combination of hydrogen bonding, π–cation, and noncovalent hydrophobic/π interactions.

In the 4I22 structure, both 3b and 3d formed a hydrogen bond with Lys745, a π–π interaction with Phe723, a π–sulfur interaction with Met790, and a π–σ interaction with Val726. Additional hydrophobic (alkyl/π–alkyl) interactions with Leu718, Ala743, Leu844, and Arg841 contributed to ligand stabilization, and in 3d, the chlorine substituent also contacted Leu792 and Met793 (Figure 5). In comparison, gefitinib engaged several of the same residues (Leu718, Ala743, Val726, Lys745, Met790, and Leu844) through different interaction types and was additionally anchored by the canonical hydrogen bond with the hinge residue Met793. Van der Waals contacts with Cys797 and Asp800 were also observed for the designed compounds; because they lack an electrophilic group, these contacts reflect a noncovalent binding mode rather than covalent engagement of Cys797. These patterns suggest that the scaffold can be accommodated within the modeled L858R/T790M pocket mainly through hydrophobic/π interactions and a Lys745 hydrogen bond, rather than through the classical hinge-region hydrogen bond formed by gefitinib.

In the 6LUD structure, compound 3b was stabilized mainly through hydrophobic and π-related interactions, including a π–π interaction with Phe723, a π–sulfur interaction with Met790, a π–σ interaction with Leu844, and an alkyl/π–alkyl interaction with Leu718 (Figure 6). Compound 3d showed a similar interaction pattern with these residues and additionally formed a hydrogen bond with Ser797, which corresponds to the C797S substitution in this mutant; this contact indicates that the designed compounds can interact with the mutated residue through a noncovalent mechanism without requiring covalent bond formation with Cys797. Both olmutinib and osimertinib exhibited hydrophobic and π-related interactions with residues in the binding pocket, including Leu718, Phe723, and Val726. Van der Waals contacts with

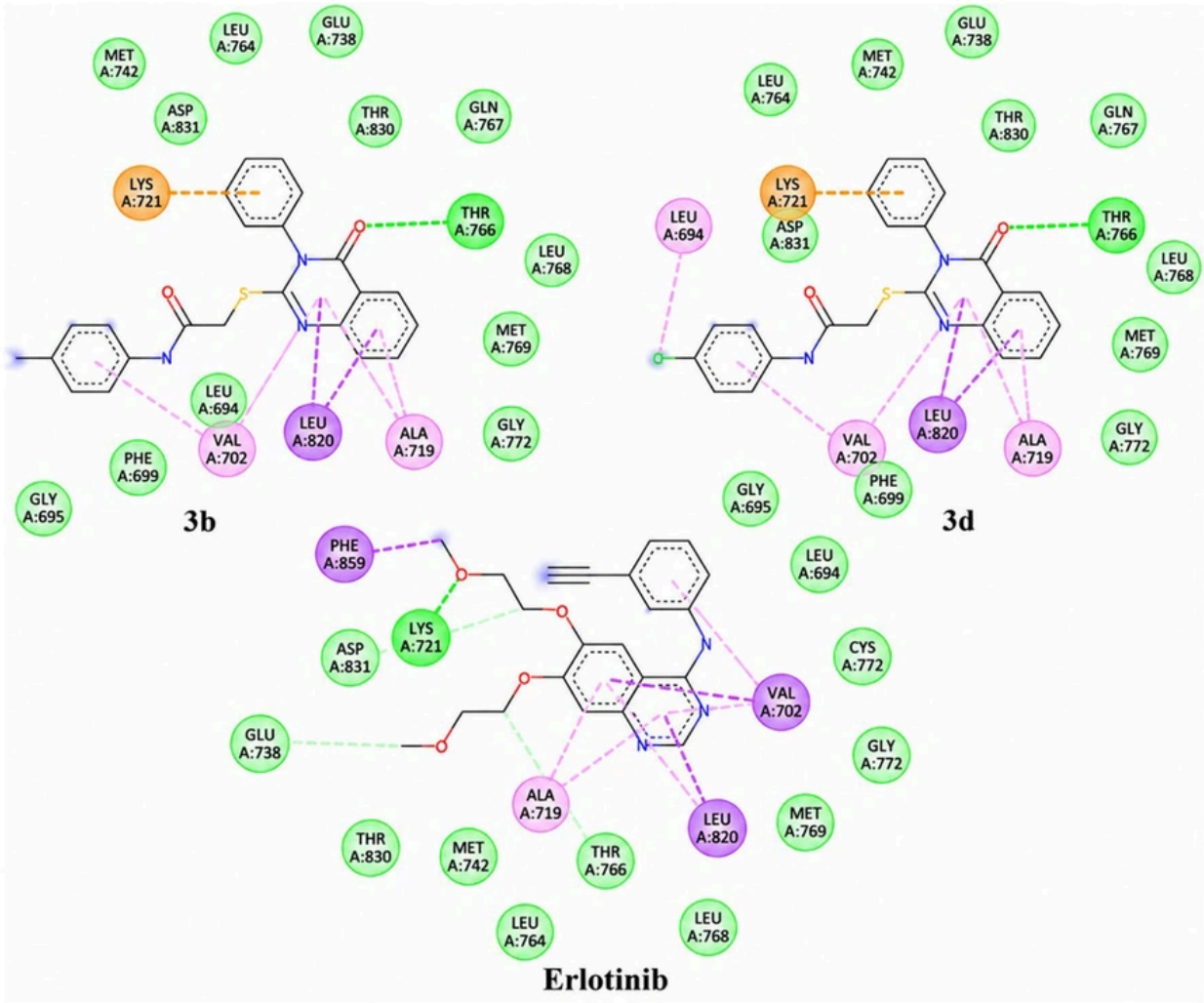


Figure 4. Predicted binding interactions of compounds 3b and 3d compared with erlotinib in wild-type EGFR (PDB ID: 1M17)

Met793, Lys745, Thr854, and Asp855 were also observed for the designed compounds. These patterns suggest that the scaffold can be accommodated within the modeled L858R/T790M/C797S pocket mainly through hydrophobic/π interactions and, for 3d, a hydrogen bond with Ser797. This is consistent with the noncovalent binding mode proposed for this series, although these results support only plausible binding capability, rather than confirmed inhibitory activity against the C797S variant (10, 11, 24, 25).

Overall, the docking results indicated that compounds 3a–3k can adopt plausible binding orientations within the ATP-binding region of the three EGFR models and form favorable noncovalent interactions, consistent with previous reports on quinazolinone-based EGFR inhibitors (12-16, 17, 23, 27). Notably, compounds 3b and 3d, which showed the most prominent cytotoxic activity, also displayed favorable predicted binding scores across the three EGFR structures. In the C797S-containing mutant model, both compounds yielded more negative docking scores than olmutinib, whereas 3k showed a comparable score. However, docking scores did not directly correspond to cytotoxic activity; for example, 3a yielded the most negative score against 4I22 and 3e against 1M17, whereas 3b and 3d showed the most favorable overall cytotoxic profiles. This discrepancy indicates that docking results alone cannot explain or reliably predict cellular

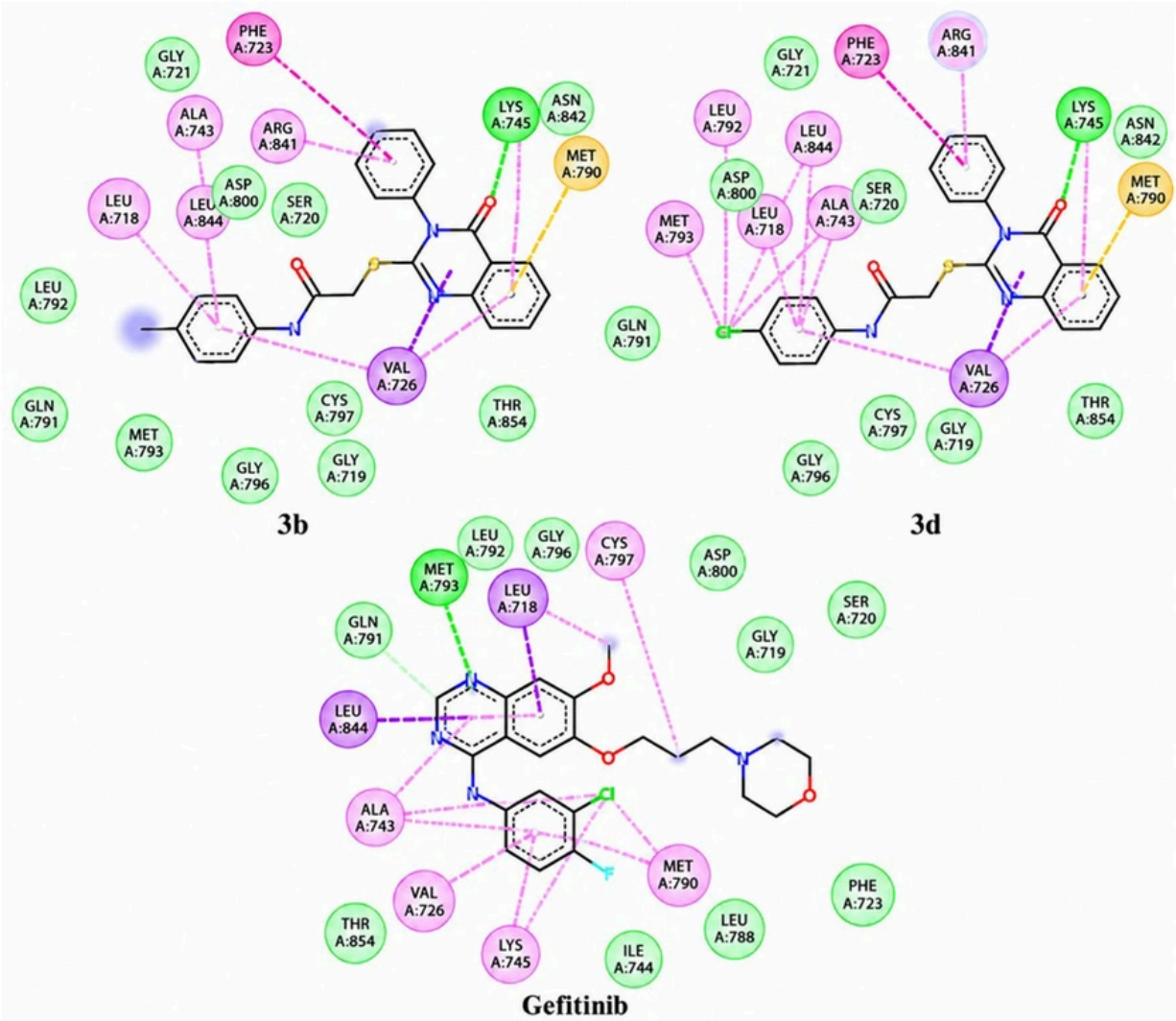


Figure 5. Predicted binding interactions of compounds 3b and 3d compared with gefitinib in EGFR L858R/T790M (PDB ID: 4I22)

cytotoxicity, which may also be influenced by solubility, stability, membrane permeability, intracellular distribution, metabolism, and interactions with other molecular targets. Although the docking results suggest that the quinazolinone–thioacetamide scaffold may be accommodated within the EGFR ATP-binding region through noncovalent interactions, they do not establish direct EGFR inhibition or an EGFR-dependent mechanism of cytotoxicity. Furthermore, EGFR expression and mutation status were not experimentally characterized in the MCF-7, HepG2, HT-29, and A549 cell lines used in this study. Therefore, the contribution of EGFR to the observed cytotoxic effects remains uncertain. Further investigations, including assessment of EGFR expression and mutation status, biochemical EGFR kinase inhibition assays, and cellular target-engagement or pathway analyses, are required to clarify the potential involvement of EGFR in the activity of these compounds.

5. Conclusions

In this study, a series of thioacetamide-linked quinazolinone derivatives was designed based on the structural features of the third-generation epidermal

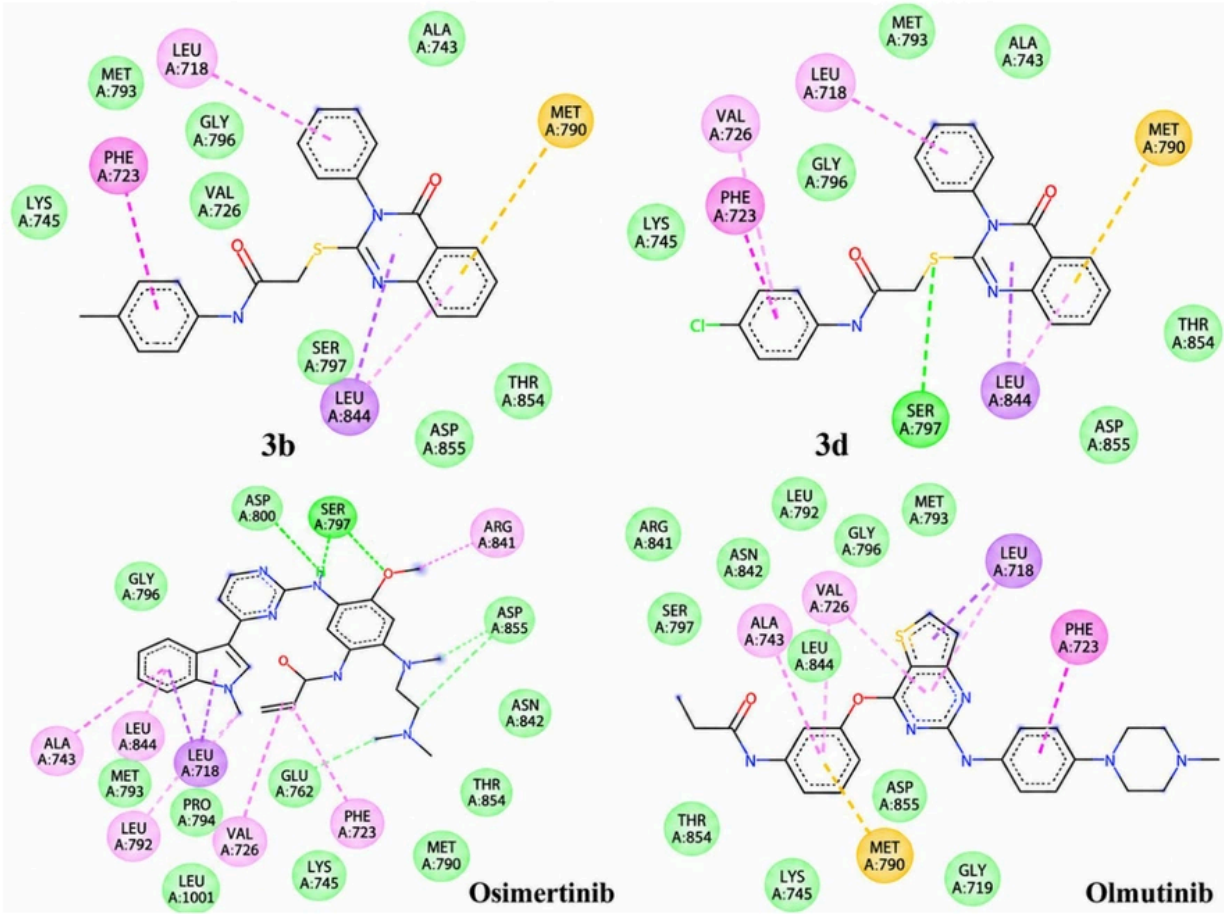


Figure 6. Predicted binding interactions of compounds 3b and 3d compared with olmutinib and osimertinib in EGFR L858R/T790M/C797S (PDB 6LUD)

growth factor receptor (EGFR) inhibitor olmutinib, synthesized, and evaluated for cytotoxic activity against four human cancer cell lines (MCF-7, HepG2, HT-29, and A549) and normal human dermal fibroblasts (HDF). Among the synthesized compounds, 3b and 3d exhibited the most favorable overall cytotoxic profiles, particularly against MCF-7 cells, and showed comparatively favorable selectivity indices in selected cell lines. These findings provide preliminary structure–activity insights under the 24-h treatment conditions used in this study. Further evaluation using longer exposure periods, additional nonmalignant cell models, and independent biological replicates is needed to better characterize their cytotoxicity and selectivity. Molecular docking studies using wild-type EGFR and the L858R/T790M and L858R/T790M/C797S mutant structures suggested that the synthesized derivatives could adopt plausible binding poses within the modeled ATP-binding region through noncovalent interactions. In the C797S-containing EGFR model, compounds 3b and 3d produced more negative docking scores than olmutinib, whereas compound 3k showed a score comparable to that of osimertinib. However, these score differences should not be interpreted as evidence of stronger binding affinity or greater inhibitory activity, as docking scores provide computational estimates rather than experimental measurements. Moreover, docking scores obtained from different EGFR structures should not be directly compared as quantitative measures of ligand affinity across receptor models. These findings should therefore be considered preliminary computational observations that require experimental validation. Overall, the findings identify the thioacetamide-linked

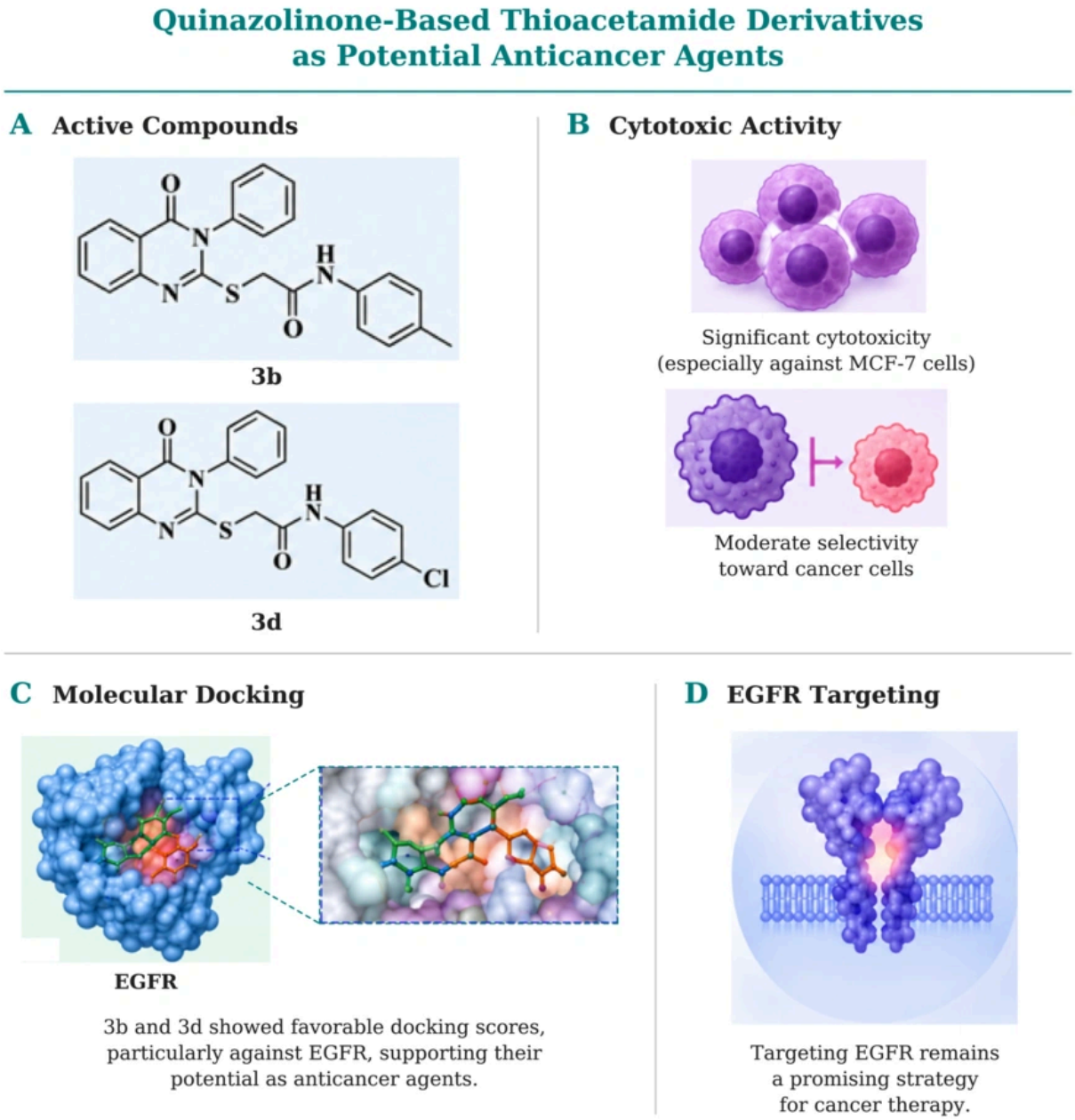


Figure 7. Graphical summary of the anticancer potential of quinazolinone-based thioacetamide derivatives. Compounds 3b and 3d demonstrated significant cytotoxic activity, particularly against MCF-7 breast cancer cells, with moderate selectivity toward cancer cells. Molecular docking analysis revealed favorable binding interactions with epidermal growth factor receptor (EGFR), supporting their potential as promising candidates for further anticancer drug development.

quinazolinone scaffold as a framework worthy of further anticancer research. However, EGFR expression and mutation status were not experimentally characterized in the investigated cell lines, and direct EGFR kinase

inhibition and cellular target engagement were not assessed. Consequently, the contribution of EGFR to the observed cytotoxic effects remains undetermined. Further studies involving EGFR profiling, biochemical kinase inhibition assays, and cellular mechanistic analyses are required to clarify the potential role of EGFR and assess the suitability of these compounds for further development. The key findings of this study, highlighting the cytotoxic activity, molecular docking interactions, and potential anticancer effects of the most promising quinazolinone-based thioacetamide derivatives, are summarized in the graphical abstract (Figure 7).

Footnotes

AI Use Disclosure: Claude was used as an AI-assisted tool to design the figure in the Graphical Abstract. The authors reviewed and approved the final figure and take full responsibility for its content.

Authors' Contribution: Study concept and design: F.K., E.R., and S.A.T.; data acquisition: S.M., R.S.A., and S.Al.T.; data analysis and interpretation: S.M., R.S.A., and S.Al.T.; manuscript drafting: S.M., R.S.A., and S.Al.T.; statistical analysis: R.S.A.; administrative, technical, and material support: F.K. and E.R.; study supervision: F.K., E.R., and S.A.T.

Conflict of Interests Statement: The authors serve as editors or editorial board members of the journal. They had no involvement in the editorial handling or peer review of this manuscript. The authors declare no other conflicts of interest.

Data Availability: All instrumental analysis results are provided in the Supplementary Materials. Any additional supporting data or information are available from the corresponding author upon reasonable request.

Ethical Approval: Ethical approval was obtained from the Ethics Committee of Shahid Beheshti University of Medical Sciences (IR.SBMU.PHARMACY.REC.1405.073).

Funding/Support: The authors thank Shahid Beheshti University of Medical Sciences for financial support through Grant No. 43020315.

Informed Consent: Informed consent was not applicable because the study did not involve human participants.

References

1. Sigismund S, Avanzato D, Lanzetti L. Emerging functions of the EGFR in cancer. *Mol Oncol*. 2018;**12**(1):3-20. [PubMed ID: 29124875]. [PubMed Central ID: PMC5748484]. https://doi.org/10.1002/1878-0261.12155.
2. Yarden Y, Pines G. The ERBB network: At last, cancer therapy meets systems biology. *Nat Rev Cancer*. 2012;**12**(8):553-563. [PubMed ID: 22785351]. https://doi.org/10.1038/nrc3309.
3. Mansournia A, Nobari N, Ghanbary F, Khezri B. Selective toxicity of iron, manganese oxide nanostructure and laser wave on colorectal and breast cancer cell. *Iran J Pharm Res*. 2025;**24**(1). e157301. [PubMed ID: 40718436]. [PubMed Central ID: PMC12296716]. https://doi.org/10.5812/ijpr-157301.
4. Ahmadabadi MN, Rezaee E, Nematpour M, Karami L, Mokhtari S, Kobarfard F, et al. Synthesis, molecular dynamics simulation, and in-vitro antitumor activity of quinazoline-2, 4, 6-triamine derivatives as novel EGFR tyrosine kinase inhibitors. *Iran J Pharm Res*. 2022;**21**(1). e133840. [PubMed ID: 36915409]. [PubMed Central ID: PMC10008000]. https://doi.org/10.5812/ijpr-133840.
5. Nagpure NR, Patel HM. Overcoming triple mutant EGFR-tyrosine kinase barriers in the therapeutics of non-small cell lung cancer: A patent review on fourth-generation inhibitors (2017–2024). *Expert Opin Ther Pat*. 2025;**35**(9):963-982. [PubMed ID: 40667612]. https://doi.org/10.1080/13543776.2025.2536006.
6. Bhatia P, Sharma V, Alam O, Manaithiya A, Alam P, Kahksha, et al. Novel quinazoline-based EGFR kinase inhibitors: A review focussing on SAR and molecular docking studies (2015-2019). *Eur J Med Chem*. 2020;**204**:112640. [PubMed ID: 32739648]. https://doi.org/10.1016/j.ejmech.2020.112640.
7. Abkhiz S, Tarighi P, Azizian H. Dual inhibitors of c-MET and EGFR in triple negative breast cancer: Pharmacophore modeling and molecular dynamics based in silico drug repositioning. *Iran J Pharm Res*. 2025;**24**(1). e164183. [PubMed ID: 41234389]. [PubMed Central ID: PMC12606863]. https://doi.org/10.5812/ijpr-164183.
8. Zhou F, Guo H, Xia Y, Le X, Tan DSW, Ramalingam SS, et al. The changing treatment landscape of EGFR-mutant non-small-cell lung cancer. *Nat Rev Clin Oncol*. 2025;**22**(2):95-116. [PubMed ID: 39614090]. https://doi.org/10.1038/s41571-024-00971-2.
9. Jia Y, Yun CH, Park E, Ercan D, Manuia M, Juarez J, et al. Overcoming EGFR (T790M) and EGFR (C797S) resistance with mutant-selective allosteric inhibitors. *Nature*. 2016;**534**(7605):129-132. [PubMed ID: 27251290]. [PubMed Central ID: PMC4929832]. https://doi.org/10.1038/nature17960.
10. Günther M, Lategahn J, Juchum M, Döring E, Keul M, Engel J, et al. Trisubstituted pyridinylimidazoles as potent inhibitors of the clinically resistant L858R/T790M/C797S EGFR mutant: Targeting of both hydrophobic regions and the phosphate binding site. *J Med Chem*. 2017;**60**(13):5613-5637. [PubMed ID: 28603991]. https://doi.org/10.1021/acs.jmedchem.7b00316.
11. Lee S, Kim J, Duggirala KB, Go A, Shin I, Cho BC, et al. Allosteric inhibitor TREA-0236 containing non-hydrolysable quinazoline-4-one for EGFR T790M/C797S mutants inhibition. *Bull Korean Chem Soc*. 2018;**39**(7):895-898. https://doi.org/10.1002/bkcs.11491.
12. Ahmed MF, Belal A, Youns M. Design, synthesis, molecular modeling and anti-breast cancer activity of novel quinazolin-4-one derivatives linked to thiazolidinone, oxadiazole or pyrazole moieties. *Med Chem Res*. 2015;**24**(7):2993-3007. https://doi.org/10.1007/s00044-015-1357-1.
13. Ahmed MF, Belal A. Design, synthesis, and molecular docking studies of 2-(furan-2-yl) quinazolin-4-one derivatives as potential antiproliferative agents. *Arch Pharm (Weinheim)*. 2015;**348**(7):487-497. [PubMed ID: 25921702]. https://doi.org/10.1002/ardp.201400468.
14. Al-Suwaidan IA, Abdel-Aziz AA, Shawer TZ, Ayyad RR, Alanazi AM, El-Morsy AM, et al. Synthesis, antitumor activity and molecular docking study of some novel 3-benzyl-4 (3H) quinazolinone analogues. *J Enzyme Inhib Med Chem*. 2016;**31**(1):78-89. [PubMed ID: 25815668]. https://doi.org/10.3109/14756366.2015.1004059.
15. Nematpour M, Rezaee E, Nazari M, Hosseini O, Tabatabai SA. Targeting EGFR tyrosine kinase: Design, synthesis and biological evaluation of novel quinazolinone derivatives. *Iran J Pharm Res*.

2022;**21**(1). e123826. [PubMed ID: 35765503]. [PubMed Central ID: PMC9191221]. https://doi.org/10.5812/ijpr.123826.

16. Ahmadabadi MN, Rezaee E, Mokhtari S, Garmabdari A, Moghadam MAJ, Kobarfard F, et al. Triazole-substituted quinazoline derivatives as novel EGFR tyrosine kinase inhibitors: Synthesis, biological evaluation, and molecular modeling. *J Mol Struct*. 2026;**1371**. 146499. https://doi.org/10.1016/j.molstruc.2026.146499.
17. Ansari SA, Deshmukh SU, Patil RB, Damale MG, Patil RH, Alkahtani HM, et al. Identification of promising biofilm inhibitory and cytotoxic quinazolin-4-one derivatives: Synthesis, evaluation, molecular docking and ADMET studies. *ChemistrySelect*. 2019;**4**(12):3559-3566. https://doi.org/10.1002/slct.201803795.
18. Sonousi A, Hassan RA, Osman EO, Abdou AM, Emam SH. Design and synthesis of novel quinazolinone-based derivatives as EGFR inhibitors with antitumor activity. *J Enzyme Inhib Med Chem*. 2022;**37**(1):2644-2659. [PubMed ID: 36146940]. [PubMed Central ID: PMC9518264]. https://doi.org/10.1080/14756366.2022.2118735.
19. Al-Majidi SMH, Al-Khuzaie MGA. Synthesis and antimicrobial activity of some new S-substituted quinazolinones containing different heterocyclic rings. *Asian Journal of Chemistry*. 2015;**27**(2):756-762. https://doi.org/10.14233/ajchem.2015.18417.
20. Lü L, Zhang L, Wai MS, Yew DT, Xu J. Exocytosis of MTT formazan could exacerbate cell injury. *Toxicol In Vitro*. 2012;**26**(4):636-644. [PubMed ID: 22401948]. https://doi.org/10.1016/j.tiv.2012.02.006.
21. Stockert JC, Blázquez-Castro A, Cañete M, Horobin RW, Villanueva A. MTT assay for cell viability: Intracellular localization of the formazan product is in lipid droplets. *Acta Histochem*. 2012;**114**(8):785-796. [PubMed ID: 22341561]. https://doi.org/10.1016/j.acthis.2012.01.006.
22. van Tonder A, Joubert AM, Cromarty AD. Limitations of the 3-(4, 5-dimethylthiazol-2-yl)-2, 5-diphenyl-2H-tetrazolium bromide (MTT) assay when compared to three commonly used cell enumeration assays. *BMC Res Notes*. 2015;**8**(1):47. [PubMed ID: 25884200]. [PubMed Central ID: PMC4349615]. https://doi.org/10.1186/s13104-015-1000-8.
23. Le Y, Gan Y, Fu Y, Liu J, Li W, Zou X, et al. Design, synthesis and in vitro biological evaluation of quinazolinone derivatives as EGFR inhibitors for antitumor treatment. *J Enzyme Inhib Med Chem*. 2020;**35**(1):555-564. [PubMed ID: 31967481]. [PubMed Central ID: PMC7006757]. https://doi.org/10.1080/14756366.2020.1715389.
24. Li Q, Zhang T, Li S, Tong L, Li J, Su Z, et al. Discovery of potent and noncovalent reversible EGFR kinase inhibitors of EGFRL858R/T790M/C797S. *ACS Med Chem Lett*. 2019;**10**(6):869-873. [PubMed ID: 31223440]. [PubMed Central ID: PMC6580378]. https://doi.org/10.1021/acsmedchemlett.8b00564.
25. Lategahn J, Keul M, Klövekorn P, Tumbrink HL, Niggenaber J, Müller MP, et al. Inhibition of osimertinib-resistant epidermal growth factor receptor EGFR-T790M/C797S. *Chem Sci*. 2019;**10**(46):10789-10801. [PubMed ID: 31857889]. [PubMed Central ID: PMC6886544]. https://doi.org/10.1039/c9sc03445e.
26. Truong DT, Ho K, Nhi HTY, Nguyen VH, Dang TT, Nguyen MT. Imidazole [1, 5-a] pyridine derivatives as EGFR tyrosine kinase inhibitors unraveled by umbrella sampling and steered molecular dynamics simulations. *Sci Rep*. 2024;**14**(1):12218. [PubMed ID: 38806555]. [PubMed Central ID: PMC11133355]. https://doi.org/10.1038/s41598-024-62743-3.
27. Al-Anazi M, Khairuddean M, Al-Najjar BO, Alidmat MM, Kamal NN, Muhamad M. Synthesis, anticancer activity and docking studies of pyrazoline and pyrimidine derivatives as potential epidermal growth factor receptor (EGFR) inhibitors. *Arab J Chem*. 2022;**15**(7). 103864. https://doi.org/10.1016/j.arabjc.2022.103864.